

Insights to Oxygen Vacancy Engineering of TiO₂ Anode for Sodium-Ion Batteries

Qi Wang,^[a] Hao Teng,^[a] Xinxin Wang,^[a] Xuelin Yang,^[a] Dan Sun,^[a] Yougen Tang,*^[a] and Haiyan Wang*^[a]

Rational construction of oxygen vacancies in electrode materials can effectively enhance the comprehensive sodium storage performance of the material. However, how to precisely control and regulate the oxygen vacancies concentration remains to be investigated, and the impact on electrochemical performance is still unclear. Herein, TiO₂ nanoparticles with tunable oxygen vacancies concentrations are used as research models, which were fabricated through a simple and effective plasma method. The experimental results reveal that a moderate concentration of oxygen vacancies can significantly improve the electrochemical kinetics and charge conductivity of the TiO₂ electro-

des. In addition, oxygen vacancies promote the release of fluorine from the fluoroethylene carbonate (FEC) in the electrolyte, inducing a NaF-rich solid electrolyte interphase, thus ensuring interfacial stability and inhibiting excessive electrolyte decomposition. Consequently, the well-designed anode exhibits outstanding rate capability (147 mAh g⁻¹ at 5 A g⁻¹) and extremely stable cycling performance (nearly 100%, 3000 cycles). This work provides a feasible method for realizing defect concentration modulation in energy storage materials and offers new insights into interfacial chemistry for improving battery performance.

Introduction

Sodium-ion batteries (SIBs) exhibit unprecedented potential for low-speed electric vehicles and grid-scale energy storage owing to their abundant sodium resources and cost-effectiveness.^[1] The development of advanced electrode materials is essential for the further development of stable high-energy SIBs.^[2] Titanium dioxide (TiO₂) has emerged as a potential alternative because of its high specific capacity, large source abundance, and environmental friendliness.^[3] Unfortunately, the inherent semiconductor characteristics and sluggish ions diffusion kinetics still hinder the advancement of SIBs.^[4]

To address these scientific issues, substantial attempts have been proposed, such as carbonaceous combining,^[5] nano-structures designing,^[6] heteroatom doping,^[7] and defect engineering.^[8] Recently, vacancy engineering, especially oxygen vacancy, has aroused great research enthusiasm in many fields.^[9] Researchers have verified that vacancy defects can alter the atomic distribution of nanomaterials and modulate their surface properties, which can significantly optimize the electronic structure of materials, eventually improving the adsorption of alkali ions.^[10] Therefore, oxygen vacancy has been used to improve the electronic conductivity and the reaction kinetics of TiO₂, thereby enhancing the sodium storage capacity.^[3a,4] For

example, the oxygen deficient, self-organized TiO_{2-x}-C NTs exhibited significantly improved electrochemical performance when used as lithium-ion or sodium-ion anodes.^[11] Despite the evident improvement in electrochemical performance achieved by vacancy engineering, the precise control of oxygen vacancies concentration in the material has not yet attracted much attention due to synthetic challenges.^[12] Therefore, the key to constructing a moderate oxygen vacancy concentration lies in revealing the constitutive relationship between sodium storage performance and oxygen vacancies concentration.

Additionally, recent studies have shown higher reaction energy is obtained after the introduction of defects in the electrode material, which play a catalytic role in inducing electrolyte reduction, thus significantly affecting the formation of the solid electrolyte interface.^[13] Xie et. al successfully introduced oxygen functional groups into hard carbon using O₂ plasma technology. Stabilized solid electrolyte interfaces were obtained thanks to the interaction between the oxygen functional groups and electrolytes, which reduced the continuous consumption of electrolytes and achieved high cycling stability.^[14] In addition, phosphorus nanocrystals were embedded into the Fe-N-C-rich three-dimensional carbon frameworks, and a NaF-rich solid electrolyte interface appeared due to the accelerated release of fluorine from the electrolyte by the Fe-N-C catalytic site.^[15] Noticeably, the strong and uncontrolled catalytic reduction on electrolytes can induce the formation of thicker SEI, which limits ion diffusion and results in poor battery cycling performance.^[16] The current consensus is to construct a thin and stable SEI layer with an inorganic inner layer and an organic outer layer. Therefore, the controlled and selective catalytic reduction of electrolytes through defect engineering is essential. In this regard, it is commonplace to modulate the interfacial chemistry of carbon materials by controlling the concentration of defects, and as far as we know, fewer studies

[a] Q. Wang, H. Teng, X. Wang, X. Yang, Prof. Dr. D. Sun, Prof. Dr. Y. Tang, Prof. Dr. H. Wang
Hunan Provincial Key Laboratory of Chemical Power Sources, College of Chemistry and Chemical Engineering
Central South University
Changsha 410083, P. R. China
E-mail: ygtang@csu.edu.cn
wanghy419@csu.edu.cn

 Supporting information for this article is available on the WWW under <https://doi.org/10.1002/batt.202400202>

have been conducted on titanium dioxide. Therefore, we focused on the effect of oxygen vacancies in TiO_2 on interfacial chemistry.

Herein, we develop a one-step argon plasma approach to fabricate a series of TiO_2 nanoparticles with different oxygen vacancy concentrations through adjusting the amount of argon.

Moreover, the underlying reasons for the improved sodium storage performance of the material have been thoroughly investigated. The results show that the oxygen defects play a dual role in the electrodes. First, the generation of electrochemically active sites facilitates the realization of high storage capacity. Second, oxygen vacancies induce electrolyte reduction and produce Na^+ electrically enhanced solid electrolyte interface.

Results and Discussion

In this work, the defective TiO_2 materials were synthesized by an Ar-plasma treatment, and the specific procedure is described in the experimental section. It is reported that high-energy radicals will attack the matrix material during plasma treatment, and various reactions take place during the energy exchange, thus imparting new properties to the material.^[17] Therefore, it is possible to achieve a great modulation of the surface properties of the material by changing the process parameters. As seen in Figure 1a, XRD patterns of all samples show no significant changes and are well assigned to the standard card of anatase TiO_2 phase (JCPDS No. 21-1272), revealing that the bulk crystal phases of TiO_2 are not obviously changed after the oxygen vacancy incorporation. In the Raman spectra (Figure 1b), all samples exhibit typical vibrational bands of anatase TiO_2 , especially the magnified E_g peaks show obvious blue-shift and intensity attenuation after Ar plasma treatment, reflecting the

reduced bonding symmetry of Ti–O, which could be ascribed to the crystallization degradation caused by the induced defects.^[3b]

XPS was conducted to determine the surface chemical states of prepared samples. The two peaks located at 529.9 and 531.7 eV in the O 1s spectrum (Figure 1d) can be attributed to the lattice oxygen and oxygen vacancy.^[18] The O 1s spectra were fitted to quantify the oxygen vacancy concentration. The results show that the concentration of oxygen vacancies increases with increasing volume of argon, and the corresponding vacancies concentrations in the TO, L-TO, M-TO, and H-TO samples are 10.6%, 12.1%, 14.2%, and 16.3%, respectively. The deconvolution of Ti 2p spectrums reveals two peaks (Figure S1), representing Ti^{4+} $2p_{3/2}$ (458.9 eV) and Ti^{4+} $2p_{1/2}$ (464.6 eV), respectively.^[19] EPR analysis was performed to further reveal the existence of oxygen vacancies in the prepared materials. The signal peaks characterized at the g value of 2.001 for L-TO, M-TO, and H-TO can be attributed to the oxygen vacancy feature (Figure 1c).^[20] Clearly, the vacancy content follows the order H-TO > M-TO > L-TO > TO, which corresponds well with the XPS analysis. The above results show that modulating the gas volume can successfully achieve the tunability of oxygen vacancy concentration in TiO_2 . SEM and TEM characterization were performed to investigate the morphology of samples. As shown in Figure 1e, f, and Figure S2, the images show that TO particles were nanosized, L-TO, M-TO, and H-TO exhibit similar morphology inherited from TO precursor, indicating that plasma treatment has no damage to the morphology. The HRTEM image for M-TO (Figure 1g) shows a lattice fringe spacing of 0.35 nm, which can be assigned to the (101) lattice plane anatase.^[3c] In addition, the EDS mappings show that elements Ti and O are evenly distributed in the M-TO samples (Figure S3).

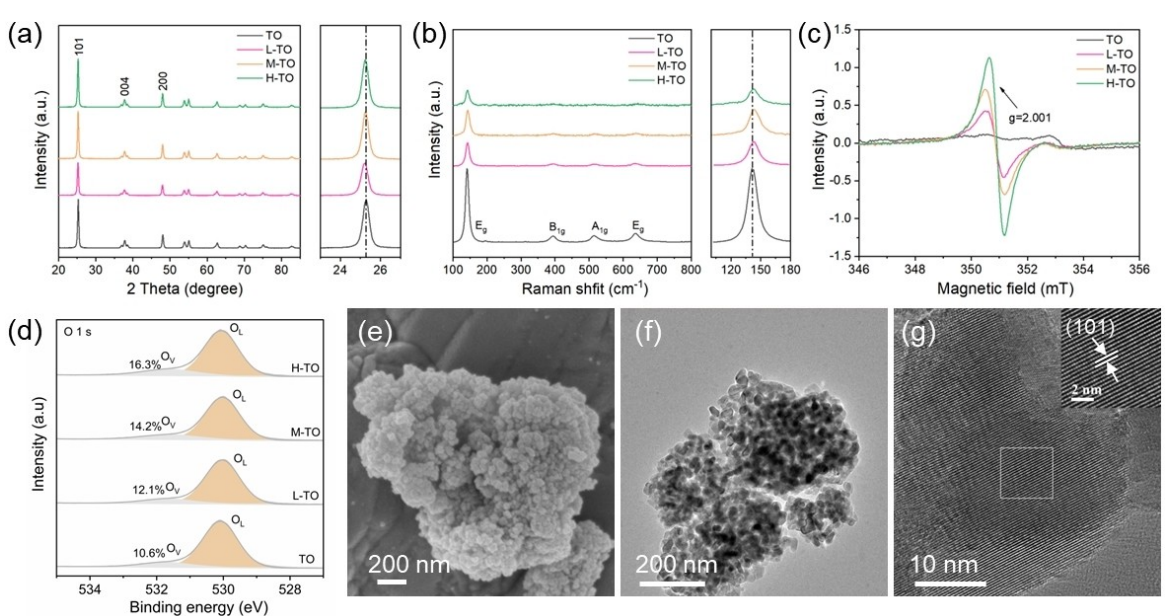


Figure 1. (a) XRD patterns and (b) Raman spectra of all samples. (c) EPR spectra of four samples. High-resolution (d) O 1s XPS spectra. (e) SEM, (f) TEM and (g) HRTEM images of M-TO.

A series of electrochemical tests were carried out to illustrate the effect of oxygen vacancy concentration on electrochemical performance. Figure 2a shows the cycling performance of the as-prepared samples at 100 mA g^{-1} . The discharge capacities of the TO, L-TO, M-TO, and H-TO after 50 cycles are maintained at 150, 170, 204, and 155 mAh g^{-1} , respectively. Figure 2b compares the rate performance of TiO_2 anodes with and without oxygen vacancy, the M-TO anode exhibits superior rate capability as the current density increases. The specific capacities of the M-TO are 183, 166, and 147 mAh g^{-1} at 1.0, 2.0, and 5.0 A g^{-1} , which is higher than many reported titanium-based anodes (Table S1).^[3c,5a,6a,7b,8b,19,21] Notably, the H-TO anode exhibits significantly reduced sodium storage capacity due to the relatively excessive oxygen vacancy concentration. It is reported that reasonable oxygen vacancy engineering can promote the electrochemical kinetics and charge conductivity of the TiO_2 anode.^[9b,d,22] The Warburg impedance of H-TO is greater than that of M-TO and L-TO (Figure S4). A high concentration of oxygen vacancies in H-TO leads to high Na^+ diffusion resistance and reduces the overall storage capacity. And M-TO can maintain similar shapes at all rates, corresponding to less polarization, further demonstrating the rapid Na^+ transfer kinetics of the electrode (Figure 2c). Figure 2d presents the cyclic stability of M-TO at a current density of 2 A g^{-1} . As seen, after 1000 cycles, the specific capacity is 171 mAh g^{-1} , and the capacity retention is almost 100%. In addition, we tested the cycling performance of the M-TO electrode at higher current densities, and it still provides excellent cycling stability (Figure S5). In order to explore the capacity contribution of conducting agent in the material, we tested the electrochemical performance of Super P (Figure S6). According to the results, the capacity contribution of Super P can be ignored. The full

cell coupling M-TO anode with $\text{Na}_3\text{V}_2(\text{PO}_4)_2\text{F}_3$ cathode was constructed to further evaluate the prospects for practical applications (relevant tests of $\text{Na}_3\text{V}_2(\text{PO}_4)_2\text{F}_3$ are displayed in Figure S7–8). The full cell delivers a reversible capacity of 61 mAh g^{-1} after 50 cycles at 20 mA g^{-1} (based on the cathode mass) and exhibits good rate performance with capacities of 46 mAh g^{-1} even at 1 A g^{-1} (Figure 2e and S9). Moreover, the electrochemical properties of the M-TO anode in THF electrolyte were also investigated. As seen, the ICE of the M-TO anode is as high as 82.9% ($267/322 \text{ mAh g}^{-1}$), which is better than many reported TiO_2 anodes (Figure S10–11).^[3b,c,5a,6–7,8b,19,23]

To further unravel the superior rate capability of the M-TO electrode, the electrochemical reaction mechanism and kinetics were carefully examined based on CV tests. As shown in Figure 3a, similar shapes are observed as the scan rate increases, indicating the slight polarization and good reversibility of M-TO.

The b-value of M-TO is 1.01 according to the equation $i = av^b$,^[24] which indicates that the sodium storage capacity is dominated by capacitive control charge (Figure 3b). The capacitive contribution of the M-TO is 82.2% at 1.0 mVs^{-1} by the equation $i = k_1v + k_2v^{1/2}$,^[11a] and it increases gradually with the increase of the scanning rate, reaching 98.5% at 4 mVs^{-1} (Figure 3c, d). Such a high capacitance contribution illustrates the ultrafast sodium storage kinetics in M-TO, demonstrating its excellent electrochemical rate performance.^[25]

The GITT was used to further investigate the fast Na^+ transport kinetics (Figure S12 illustrates the detailed calculation process). Apparently, M-TO demonstrates the highest Na^+ -diffusion coefficients during the charge/discharge process, suggesting obviously promoted sodium storage kinetics (Figure 3e, f). Temperature-dependent EIS was used to further

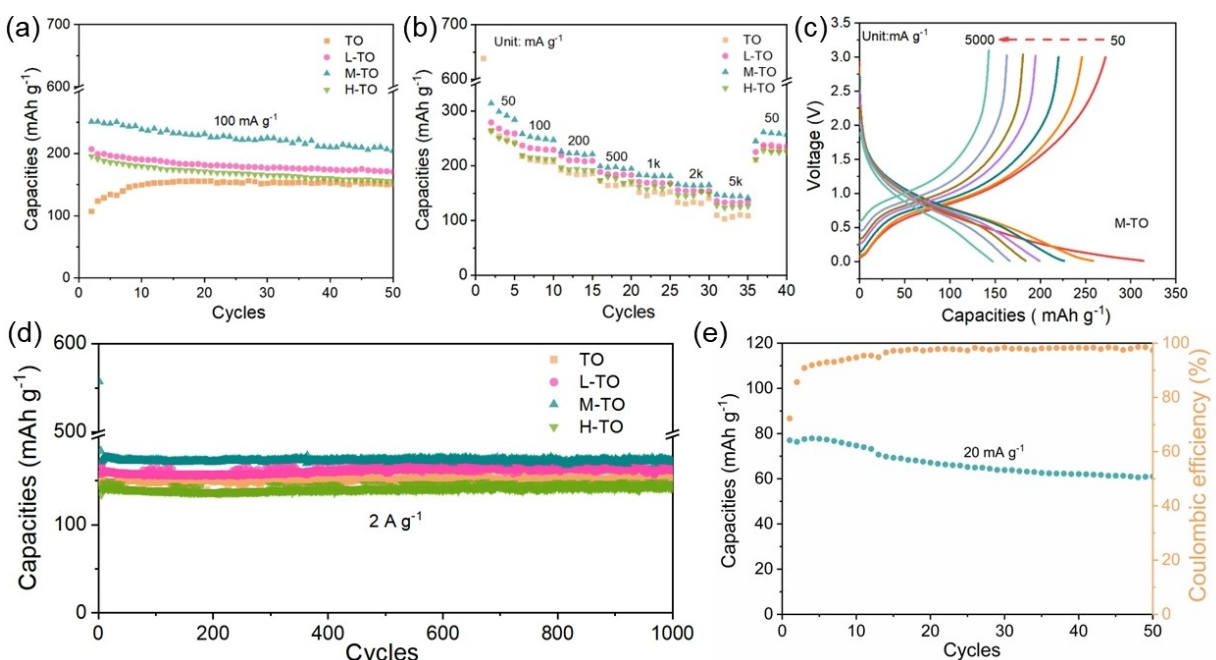


Figure 2. (a) Cycling performance of as-prepared anodes at 100 mA g^{-1} . (b) Rate performance comparison of four anodes. (c) The charge/discharge curves at varied rates of M-TO. (d) Long-term cycling performance at 2 A g^{-1} . (e) Cycling performance of the full cells.

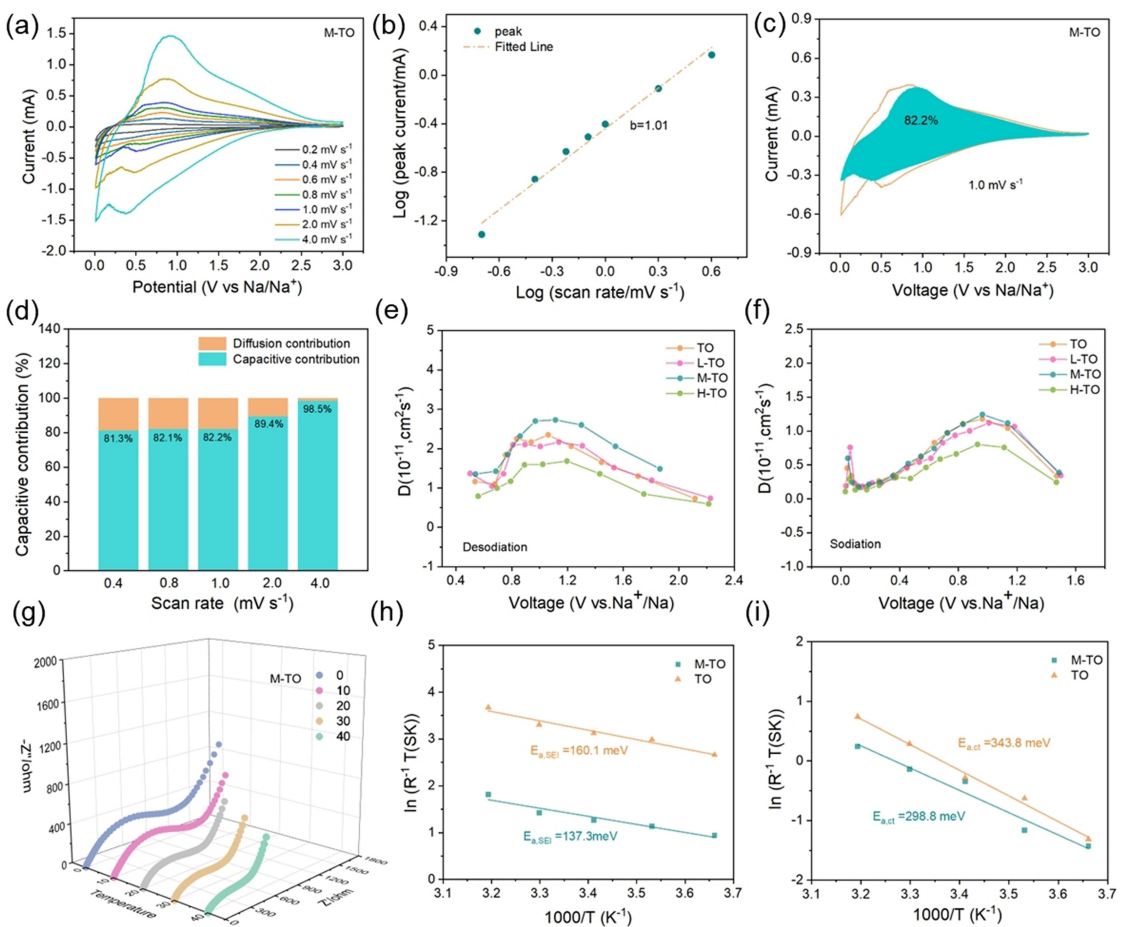


Figure 3. (a) CV curves of M-TO anodes, (b) Linear fitting of $\log(v)$ and $\log(i)$. (c) Capacitance contribution of M-TO at 1 mV s^{-1} . (d) Capacitive contribution percentages at different scanning rates. Na^+ diffusion coefficients of four anodes for (e) desodiation (f) and sodiation. (g) Nyquist plots of the M-TO anodes. Corresponding activation energies derived by Arrhenius fitting for $E_{a,SEI}$ (h) and $E_{a,ct}$ (i)

investigate the Na^+ diffusion in the SEI and charge-transfer impedance (Figure 3g and Figure S13). The activation energy are calculated by the classical Arrhenius equation (Table S2).^[16] Obviously, the $E_{a,SEI}$ and $E_{a,ct}$ of M-TO anode are lower than those of TO anode, this is attributed to the facilitated interface Na^+ diffusion kinetics after the introduction of oxygen vacancy (Figure 3 h, i). Based on the above experimental results, the M-TO electrode exhibits higher capacitance behavior, lower charge transfer impedance, and faster ion diffusion rate than other electrodes. Therefore, it can be concluded that adjusting the concentration of oxygen vacancy can favor electron transfer and ion transport.

Ex situ XRD, Raman, and XPS characterizations were performed to gain insight into the sodium storage mechanism. Figures 4a and b show the structural evolution of M-TO at different stages during the initial cycle. When discharge from open circuit voltage to 0.01 V, the XRD patterns exhibit similar shapes except for the change in the peak intensity of the characteristic peak of (101). The Raman results show that the E_g characteristic peak decreases as the discharging proceeds, during the charging process, the E_g peak recovers to the original stage (Figure 4c).^[22] The above results indicate that

the M-TO electrode has excellent reversibility and superior structural stability upon sodiation/desodiation.

The Na^+ kinetics difference between TO and M-TO is closely related to electrode/electrolyte interface stability, thus in-situ EIS was performed during the initial cycle (Figure 4d and S14b). The impedance data of each part after fitting are summarized in Table S3. By tracking the SEI resistance (R_{SEI}) of the M-TO anode at different stages (Figure 4e), it can be seen that R_{SEI} increases continuously during the discharge process and displays a major impedance drop after discharge to 0.01 V, which indicates that the SEI is rapidly formed and stabilizes quickly. During the charging process, the interface impedance of the M-TO electrodes is significantly lower than that of the TO electrodes, showing excellent ion transport properties. Notably, the impedance of M-TO decreases as the cycling proceeds, indicating a sustainably stable SEI layer on M-TO. While, a continuously surging resistance is observed for TO during cycling, which should be due to the continuous electrolyte reduction and SEI accumulation (Figure S15), leading to unsatisfactory rate performance of the TO electrode.^[13c] Figure 4f shows the evolution of the charge transfer resistance (R_{ct}) versus cycling. As seen, the R_{ct} of M-TO is also lower than that of the TO electrode, which further confirms the significant improve-

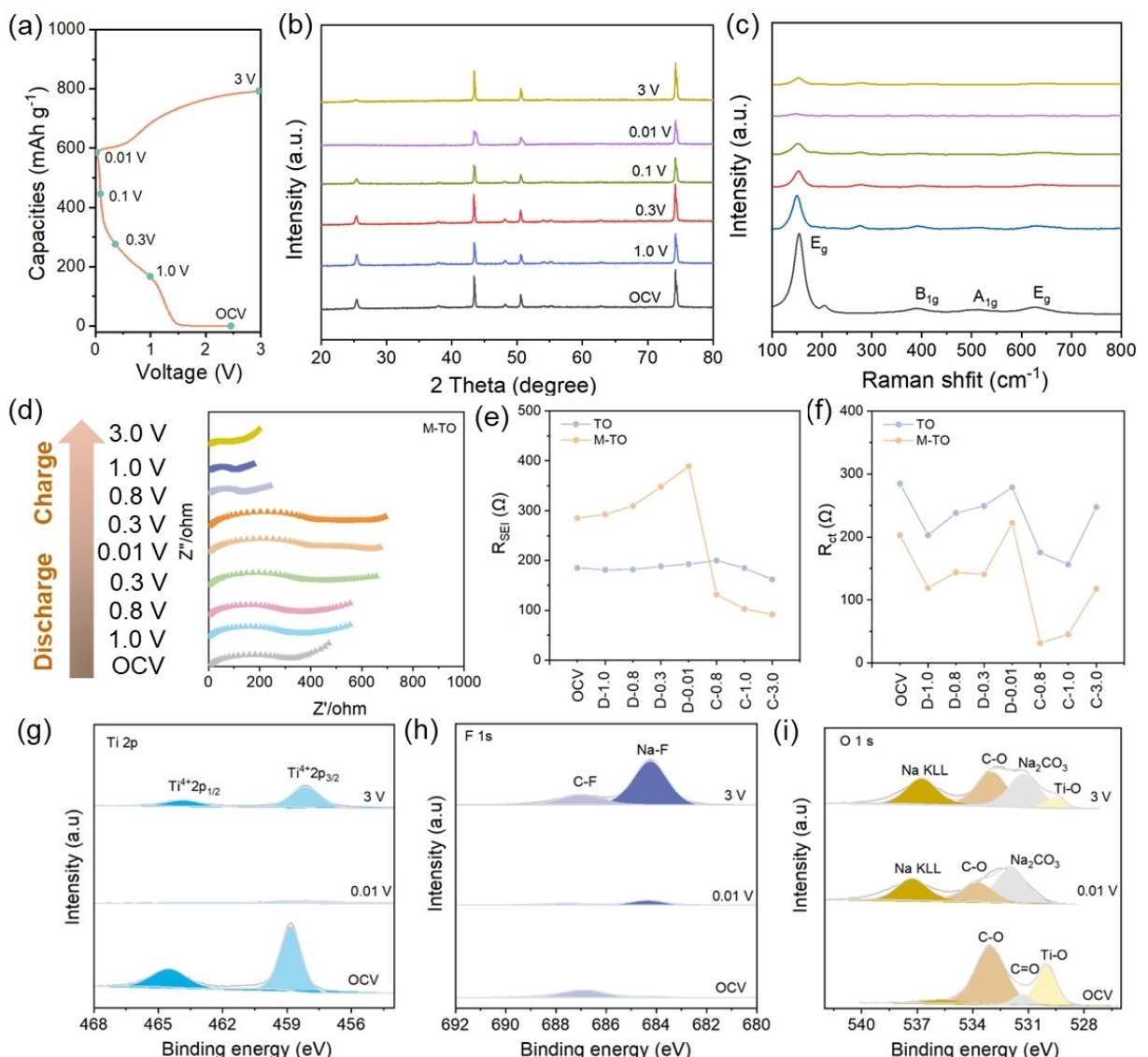


Figure 4. (a) Initial discharge/charge curves of M-TO. (b) Corresponding ex-situ XRD patterns. (c) Raman spectra. (d) Nyquist plots of M-TO at different potentials in the initial cycle. Fitted impedance values (e) R_{SEI} and (f) R_{ct} . The high-resolution spectra of (g) Ti 2p, (h) F 1s, (i) O 1s XPS of M-TO at discharging and charging states.

ment in charge transfer kinetics with the introduction of oxygen vacancies.^[1b]

The valence changes of the element Ti in the first cycle were characterized by the ex-situ XPS test. It is observed that the Ti^{4+} content decreases when discharged to 0.01 V and increases when charged to 3.0 V (Figure 4g), which further demonstrates the good reversibility of the M-TO electrode, as confirmed by the O 1s spectra (Figure 4i). Moreover, as displayed in Figure 4h, an F peak at 684.3 eV is detected for both discharge and charge, indicating the presence of NaF.^[15]

TEM and In-depth XPS were employed to characterize the structure and components of the SEI on the M-TO anode. As can be seen from Figure 5c-d, heterogeneous SEI with a thickness of 5.4 nm can be found on the M-TO electrode, which contains the inorganic substance NaF (200) along with some amorphous layers. In stark contrast, the SEI layer observed on

the TO is much thicker and not clearly delaminated (Figure 5a, b), and exists predominantly in the form of an amorphous phase, suggesting a difference in electrolyte decomposition behavior between M-TO and these electrodes.^[15] Moreover, H-TO has the thickest SEI film, which may be caused by severe electrolyte catalysis due to excess defects (Figure S16).^[11b, 26]

Depth-profiling XPS analysis was performed on the cycled electrodes. Specifically, more NaF is present throughout the inner layer with increasing etching depth, which matches well with TEM measurements (Figure 6b, Table S5). In addition, the proportion of Na_2CO_3 (289.3 eV) in M-TO is significantly lower based on C1s XPS spectra, whereas a high abundance of Na_2CO_3 component is induced in TO (Figure 6a, Figure S17, and Table S4). These friendly inorganic NaF species are highly conductive interfacial components and thus favor electrochemical kinetics. The above results reveal that the M-TO exhibits a

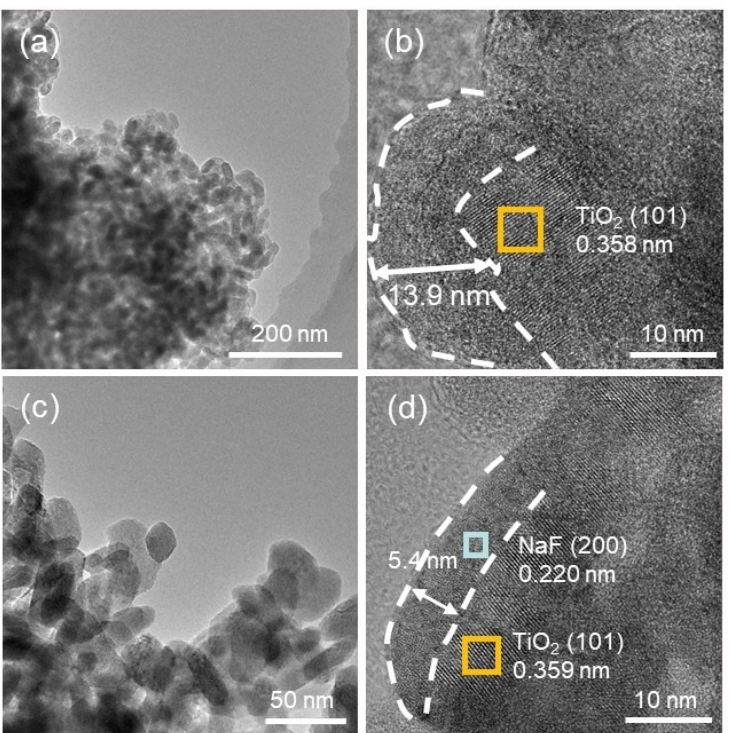


Figure 5. TEM images of (a) TO, (c) M-TO. HRTEM images of (b) TO, (d) M-TO.

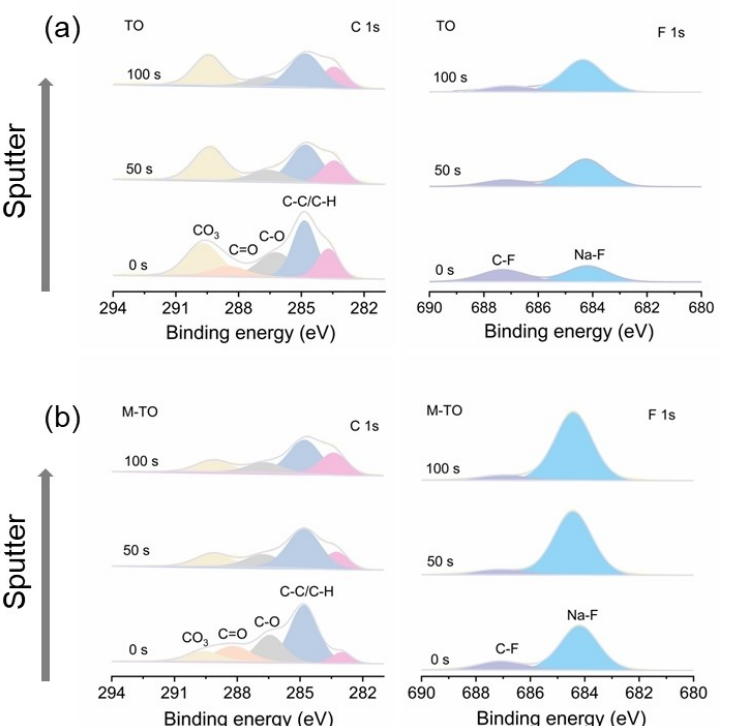


Figure 6. High-resolution XPS spectra of (a) TO and (b) M-TO at sputtering time of 0, 50, and 100 s, respectively.

more favorable catalytic effect on FEC decomposition, while more solvent reduction in TO.^[16]

In order to explore the effects of oxygen vacancies concentration on the structural stability of M-TO anodes, the morphology evolution of the electrode after different cycles

was collected using SEM and TEM. As shown in Figure 7a-f, some interesting morphological evolution occurs during the first cycle. The M-TO is distributed in the form of nanoparticles under the initial state. After discharging to 0.01 V, the nanoparticles begin to aggregate into spherical shapes of different sizes. Even after 300 cycles, the morphology remains very stable and the surface of the M-TO electrode is relatively smooth (Figure 7f). Nevertheless, the surface of the TO electrode is covered by a dense SEI layer (Figure S18), further confirming more severe electrolyte decomposition. The Na^+ transfer through the interphase interface becomes slow due to the ultra-thick SEI, thus leading to unsatisfactory sodium storage performance.^[1a] The stability of oxygen vacancy during cycling was studied by the EPR test. In Figure 7k, the EPR spectra of M-TO remain almost constant after different cycles, indicating that the oxygen vacancy has high stability. Additionally, the XPS (Figure 7i-j) and TEM (Figure 7g-h) characterization further reveal the favorable structural stability of the M-TO electrode.

According to the above results, the electrochemical performance of TiO_2 is not positively correlated with oxygen vacancy concentration. Specifically, the electrochemical performance improves with the increase of oxygen vacancy concentration, while excessive oxygen vacancies suppress the electrochemical kinetics. Therefore, it is critical to engineer oxygen vacancies when preparing defective materials. Overall, M-TO demonstrates optimal electrochemical performance for two main reasons: first, both Na^+ intercalation/de-intercalation kinetics and storage capacity are greatly improved due to the existence of oxygen vacancies. Second, oxygen vacancies may effectively promote the decomposition of FEC, this induces

NaF-rich layers and rapid formation of SEI and inhibits excessive electrolyte decomposition, thereby resulting in a highly stable interface.

Conclusions

To conclude, we successfully prepared TiO_2 nanoparticles with different oxygen vacancy concentrations by argon plasma treatment, and elucidated that keeping an optimized oxygen vacancy concentration plays a critical role in ensuring great electrochemical performance of TiO_2 . Combined with relevant characterization and electrochemical measurement, a structure–property correlation between electrochemical performance and oxygen vacancy concentration was set up. Moderate oxygen vacancy concentration can promote electrochemical kinetics and charge conductivity of TiO_2 anodes, and it can also induce the decomposition of FEC to form a NaF-rich and stable SEI, thus ensuring interfacial stability. As a result, the optimized M-TO delivers a high reversible specific capacity (314 mAh g^{-1} /0.05 Ag^{-1} , and 147 mAh g^{-1} /5 Ag^{-1}), and consistently serving >3000 cycles at 10 Ag^{-1} . This work demonstrates the effectiveness of the plasma technique in modulating the concentration of oxygen vacancies of TiO_2 anodes and can be generalized to other metal oxide materials, thus facilitating the research and development of rechargeable batteries. In addition, this study also reveals the role of oxygen-deficient catalyzed electrolyte favorable decomposition in promoting stable and fast SEI formation, which may provide enlightenment for subsequent improvement of electrode interface stability.

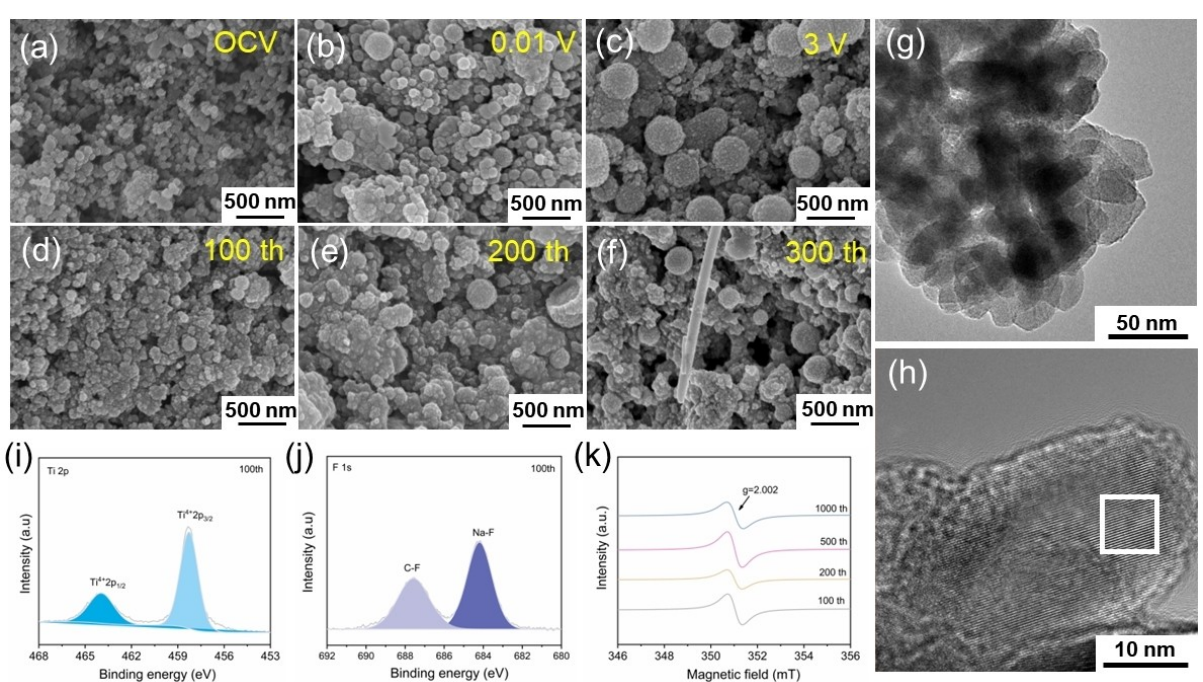


Figure 7. (a–f) SEM images of M-TO electrode after various cycles. (g) TEM, and (h) HRTEM images of M-TO anode particles after 100 cycles. XPS spectra of (i) Ti 2p and (j) F 1s after 100 cycles of the M-TO electrode. (k) EPR spectra of the M-TO sample after various cycles.

Experimental section

Material Synthesis

Commercial anatase TiO_2 was purchased from Macklin Inc. In a typical procedure, a porcelain boat with 0.2 g commercial anatase TiO_2 (named TO) was transferred to a quartz tube furnace equipped with a plasma device. Pure Ar atmosphere was used as the carrier gas with a flow rate of 20 sccm. As the reaction temperature went up to 500°C at 5°C min⁻¹, plasma was turned on with an input power of 200 W for 2 h (Plasma-Chemical Vapor Deposition System, Tianjin Zhonghuan). After that, the plasma device was turned off and the furnace was cooled to room temperature naturally to obtain the oxygen vacancy-modified TiO_2 (named M-TO). To obtain TiO_2 with various oxygen vacancy concentrations, the above experimental procedure was repeated by varying only the gas volume, i.e., 10, 30 sccm (named L-TO and H-TO, respectively).

Characterization

X-ray diffraction (XRD) patterns were recorded by an X-ray diffractometer (Japan, Rigaku Ultima IV) using Cu-K α radiation. Raman spectra were collected by Renishaw/inVia Reflex spectrometer. The morphological structure of the samples was tested by emission field scanning electron microscopy (SEM, JEOL/JSM-7610FPlus) and transmission electron microscopy (TEM, JEOL/JEM-F200). X-ray photoelectron spectrometry was used to explore the valance states of samples (XPS, ESCALAB 250Xi/Thermo Fisher Scientific, the specific details of the tests are provided in the Supporting Information). EPR spectra were acquired with a Bruker EMXplus instrument.

Electrochemical Measurements

The anode slurry was composed of 70 wt% active material, 20 wt% Super P, and 10 wt% carboxymethyl cellulose with a certain amount of deionized water. The slurry was coated on copper foil, dried under vacuum at 80°C for 10 h, and then cut into discs of 1.2 cm diameter. The mass loading of the active material was around 1.2~1.5 mg⁻¹. The Na⁺ storage performance was tested in CR2016 coin cells with the Na metal serving as the counter electrode and the glass fiber as a separator. The electrolyte was 1 M NaClO₄ in a 1:1 (v/v) mixture of EC and DMC, with 5 wt% FEC. The constant-current charge/discharge and galvanostatic intermittent titration technique (GITT) tests were carried out on the Neware battery testing system (CT-3008 W) in a voltage range of 0.01–3.0 V. Cyclic voltammetry (CV) and electrochemical impedance spectroscopy (EIS) measurements were performed on CHI602E electrochemical workstation. CR2025 full cells were assembled to evaluate the practical application value with M-TO as the anode, $\text{Na}_3\text{V}_2(\text{PO}_4)_2\text{F}_3$ as the cathode ($\text{Na}_3\text{V}_2(\text{PO}_4)_2\text{F}_3$ was synthesized according to our group's method). The voltage range was selected at 1.5–3.9 V for full cell. The M-TO anode was presodiated before assembling.

Acknowledgements

The work was financially supported by the National Nature Science Foundation of China (21975289, 21905306); the Science and Technology Innovation Program of Hunan Province (2022RC3050); and the Hunan Provincial Science and Technology Plan Project of China (2017TP1001).

Conflict of Interests

The authors declare no conflict of interest.

Data Availability Statement

Research data are not shared.

Keywords: oxygen vacancies · enhanced kinetics · interfacial chemistry · titanium dioxide · sodium-ion batteries

- [1] a) F. Cheng, M. Cao, Q. Li, C. Fang, J. Han, Y. Huang, *ACS Nano* **2023**, *17*, 18608–18615; b) W. Meng, Z. Dang, D. Li, L. Jiang, *Adv. Mater.* **2023**, *35*, 2301376; c) Z. Tang, H. Wang, P.-F. Wu, S.-Y. Zhou, Y.-C. Huang, R. Zhang, D. Sun, Y.-G. Tang, H.-Y. Wang, *Angew. Chem. Int. Ed.* **2022**, *61*, e202200475.
- [2] a) Z. Tang, R. Zhang, H. Wang, S. Zhou, Z. Pan, Y. Huang, D. Sun, Y. Tang, X. Ji, K. Amine, M. Shao, *Nat. Commun.* **2023**, *14*, 6024; b) S. Zhou, Z. Tang, Z. Pan, Y. Huang, L. Zhao, X. Zhang, D. Sun, Y. Tang, A. S. Dhemees, H. Wang, *SusMat* **2022**, *2*, 357–367; c) X. Dou, I. Hasa, D. Saurel, C. Vaalma, L. Wu, D. Buchholz, D. Bresser, S. Komaba, S. Passerini, *Mater. Today* **2019**, *23*, 87–104.
- [3] a) Q. Cai, X. Li, E. Hu, Z. Wang, P. Lv, J. Zheng, K. Yu, W. Wei, K. Ostrikov, *Small* **2022**, *18*, 2200694; b) Q. Gan, H. He, Y. Zhu, Z. Wang, N. Qin, S. Gu, Z. Li, W. Luo, Z. Lu, *ACS Nano* **2019**, *13*, 9247–9258; c) Q. Wang, Z. Tang, R. Zhang, D. Sun, L. Fu, Y. Tang, H. Li, H. Xie, H. Wang, *ACS Appl. Mater. Interfaces* **2023**, *15*, 40508–40518.
- [4] Q. Wang, S. Zhang, H. He, C. Xie, Y. Tang, C. He, M. Shao, H. Wang, *Chem. Asian J.* **2021**, *16*, 3–19.
- [5] a) Q. Zhang, H. He, X. Huang, J. Yan, Y. Tang, H. Wang, *Chem. Eng. J.* **2018**, *332*, 57–65; b) S. Yao, Y. Ma, T. Xu, Z. Wang, P. Lv, J. Zheng, C. Ma, K. Yu, W. Wei, K. Ostrikov, *Carbon* **2021**, *171*, 524–531.
- [6] a) H. He, Q. Gan, H. Wang, G.-L. Xu, X. Zhang, D. Huang, F. Fu, Y. Tang, K. Amine, M. Shao, *Nano Energy* **2018**, *44*, 217–227; b) L. Fu, Q. Wang, H. He, Y. Tang, H. Wang, H. Xie, *J. Power Sources* **2021**, *489*, 229516; c) Z. Diao, Y. Wang, D. Zhao, X. Zhang, S. S. Mao, S. Shen, *Chem. Eng. J.* **2021**, *417*, 127928.
- [7] a) C. Chen, Y. Yang, S. Ding, Z. Wei, X. Tang, P. Li, T. Wang, G. Cao, M. Zhang, *Energy Storage Mater.* **2018**, *13*, 215–222; b) H. He, D. Huang, W. Pang, D. Sun, Q. Wang, Y. Tang, X. Ji, Z. Guo, H. Wang, *Adv. Mater.* **2018**, *30*, 1801013.
- [8] a) Q. Ni, R. Dong, Y. Bai, Z. Wang, H. Ren, S. Sean, F. Wu, H. Xu, C. Wu, *Energy Storage Mater.* **2020**, *25*, 903–911; b) Q. Wang, H. He, J. Luan, Y. Tang, D. Huang, Z. Peng, H. Wang, *Electrochim. Acta* **2019**, *309*, 242–252.
- [9] a) J. Li, Y. Wang, X. Lu, K. Guo, C. Xu, *Inorg. Chem.* **2022**, *61*, 17242–17247; b) Y. Du, X. Wang, J. Sun, *Nano Res.* **2021**, *14*, 754–761; c) L. Ma, Y. Zhang, S. Zhang, L. Wang, C. Zhang, Y. Chen, Q. Wu, L. Chen, L. Zhou, W. Wei, *Adv. Funct. Mater.* **2023**, *33*, 2305788; d) J.-H. Li, Y.-X. Yu, *ChemSusChem* **2021**, *14*, 5488–5498.
- [10] a) M. Choi, W. Lee, *Chem. Eng. J.* **2022**, *431*, 134345; b) Y. Zhang, L. Tao, C. Xie, D. Wang, Y. Zou, R. Chen, Y. Wang, C. Jia, S. Wang, *Adv. Mater.* **2020**, *32*, 1905923; c) Q. Cheng, M. Huang, L. Xiao, S. Mou, X. Zhao, Y. Xie, G. Jiang, X. Jiang, F. Dong, *ACS Catal.* **2023**, *13*, 4021–4029; d) S. Jin, X. Ma, J. Pan, C. Zhu, S. E. Saji, J. Hu, X. Xu, L. Sun, Z. Yin, *Appl. Catal. B* **2021**, *281*, 119477.
- [11] a) E. Portenkirchner, D. Werner, S. Liebl, D. Stock, A. Auer, J. Kunze-Liebhäuser, *ACS Appl. Energ. Mater.* **2018**, *1*, 6646–6653; b) J. Brumbarov, J. P. Vivek, S. Leonardi, C. Valero-Vidal, E. Portenkirchner, J. Kunze-Liebhäuser, *J. Mater. Chem. A* **2015**, *3*, 16469–16477.
- [12] S. Dong, N. Lv, Y. Wu, Y. Zhang, G. Zhu, X. Dong, *Nano Today* **2022**, *42*, 101349.
- [13] a) W. Song, E. S. Scholtis, P. C. Sherrell, D. K. H. Tsang, J. Ngiam, J. Lischner, S. Fearn, V. Bemmer, C. Mattevi, N. Klein, F. Xie, D. J. Riley, *Energy Environ. Sci.* **2020**, *13*, 4977–4989; b) Y. Li, M. Liu, X. Feng, Y. Li, F. Wu, Y. Bai, C. Wu, *ACS Energy Lett.* **2021**, *6*, 3307–3320; c) Y. Wan, K. Song, W. Chen, C. Qin, X. Zhang, J. Zhang, H. Dai, Z. Hu, P. Yan, C. Liu, S. Sun, S.-L. Chou, C. Shen, *Angew. Chem.* **2021**, *133*, 11582–11587; d) Y. Sun, R. Hou, S. Xu, H. Zhou, S. Guo, *Angew. Chem. Int. Ed.* **2024**, *n/a*, e202318960.

- [14] H. Xie, Z. Wu, Z. Wang, N. Qin, Y. Li, Y. Cao, Z. Lu, *J. Mater. Chem. A* **2020**, *8*, 3606–3612.
- [15] J. Ge, C. Ma, Y. Wan, G. Tang, H. Dai, S. Sun, W. Chen, *Adv. Funct. Mater.* **2023**, *33*, 2305803.
- [16] M. Liu, F. Wu, Y. Gong, Y. Li, Y. Li, X. Feng, Q. Li, C. Wu, Y. Bai, *Adv. Mater.* **2023**, *35*, 2300002.
- [17] S. Dou, L. Tao, R. Wang, S. El Hankari, R. Chen, S. Wang, *Adv. Mater.* **2018**, *30*, 1705850.
- [18] L. Mao, H. Xie, F. Wang, J. Mao, *Batteries & Supercaps* **2022**, *5*, e202100192.
- [19] Q. Gan, H. He, K. Zhao, Z. He, S. Liu, S. Yang, *ACS Appl. Mater. Interfaces* **2018**, *10*, 7031–7042.
- [20] M. Wang, G. Zhao, X. Bai, W. Yu, C. Zhao, Z. Gao, P. Lyu, Z. Chen, N. Zhang, *Adv. Energy Mater.* **2023**, *13*, 2301730.
- [21] a) S. Nie, L. Liu, J. Liu, J. Xie, Y. Zhang, J. Xia, H. Yan, Y. Yuan, X. Wang, *Nano-Micro Lett.* **2018**, *10*, 71; b) H. Wang, J. Xiong, X. Cheng, G. Chen, T. Kups, D. Wang, P. Schaaf, *Sustain. Energy Fuels* **2019**, *3*, 2688–2696; c) W. Meng, J. Han, Z. Dang, D. Li, L. Jiang, *ACS Appl. Mater. Interfaces* **2021**, *13*, 44214–44223.
- [22] W. Hou, P. Feng, X. Guo, Z. Wang, Z. Bai, Y. Bai, G. Wang, K. Sun, *Adv. Mater.* **2022**, *34*, 2202222.
- [23] a) Y. Zhang, C. Wang, H. Hou, G. Zou, X. Ji, *Adv. Energy Mater.* **2017**, *7*, 1600173; b) L. Ling, Y. Bai, Z. Wang, Q. Ni, G. Chen, Z. Zhou, C. Wu, *ACS Appl. Mater. Interfaces* **2018**, *10*, 5560–5568; c) W. Zhang, N. Luo, S. Huang, N.-L. Wu, M. Wei, *ACS Appl. Energ. Mater.* **2019**, *2*, 3791–3797; d) M. Fan, Z. Lin, P. Zhang, X. Ma, K. Wu, M. Liu, X. Xiong, *Adv. Energy Mater.* **2021**, *11*, 2003037; e) K. Li, J. Zhang, D. Lin, D.-W. Wang, B. Li, W. Lv, S. Sun, Y.-B. He, F. Kang, Q.-H. Yang, L. Zhou, T.-Y. Zhang, *Nat. Commun.* **2019**, *10*, 725; f) Z.-L. Xu, K. Lim, K.-Y. Park, G. Yoon, W. M. Seong, K. Kang, *Adv. Funct. Mater.* **2018**, *28*, 1802099; g) D. Lv, D. Wang, N. Wang, H. Liu, S. Zhang, Y. Zhu, K. Song, J. Yang, Y. Qian, *J. Energy Chem.* **2022**, *68*, 104–112.
- [24] H. He, H. Zhang, D. Huang, W. Kuang, X. Li, J. Hao, Z. Guo, C. Zhang, *Adv. Mater.* **2022**, *34*, 2200397.
- [25] a) E. Portenkirchner, S. Rommel, L. Szabados, C. Griesser, D. Werner, D. Stock, J. Kunze-Liebhäuser, *Nano Sel.* **2021**, *2*, 1533–1543; b) L. Szabados, D. Winkler, D. Stock, T. Alexander, T. Lörting, J. Kunze-Liebhäuser, E. Portenkirchner, *Adv. Energy Sustainability Res.* **2022**, *3*, 2200104.
- [26] X. Tang, F. Xie, Y. Lu, H. Mao, Z. Chen, H. Pan, S. Weng, Y. Yang, X. Li, Z. Guo, Q. Guo, F. Ding, X. Hou, Y. Li, X. Wang, M.-M. Titirici, L. Chen, Y. Pan, Y.-S. Hu, *ACS Energy Lett.* **2024**, *9*, 1158–1167.

Manuscript received: March 24, 2024

Revised manuscript received: April 30, 2024

Accepted manuscript online: May 14, 2024

Version of record online: June 25, 2024